Biomaterials Science

ROYAL SOCIETY OF CHEMISTRY

PAPER

View Article Online
View Journal | View Issue

Check for updates

Cite this: *Biomater. Sci.*, 2026, **14**, 1665

Rational design of a targeted theranostic nanoagent for sequential application during oral squamous cell carcinoma surgery

Danni Shan, †[a] Diya Xie, †[a] Liping Zeng,[a] Jianquan Wang *[b] and Zhiyong Wang*[a]

Oral squamous cell carcinoma (OSCC) is a common cancer of the head and neck, and its treatment outcome depends strongly on whether the tumor is completely removed during surgery. Current tools for preoperative imaging, intraoperative guidance, and postoperative treatment are not well connected, which makes it difficult for surgeons to accurately identify tumor margins and manage residual cancer. Here, we developed a theranostic nanoplatform called AuNPs/HSA–ICG. It is made by loading indocyanine green (ICG) and gold nanoparticles (AuNPs) onto human serum albumin (HSA). This system combines three functions in one: preoperative computed tomography (CT) imaging, intraoperative near-infrared fluorescence guidance, and postoperative photodynamic therapy (PDT). The nanoplatform shows good fluorescence stability, strong CT contrast, and specific tumor-targeting capability attributable to secreted protein acidic and rich in cysteine (SPARC)-mediated active uptake. In an orthotopic tongue cancer model, the combined CT and fluorescence imaging allowed accurate tumor localization and clear visualization of surgical margins, facilitating complete tumor removal. In a residual tumor model simulating positive margins, ICG-based PDT effectively suppressed tumor regrowth. Safety evaluations showed good biocompatibility and low systemic toxicity. Overall, this study presents a clinically translatable, integrated strategy for precise surgical margin management in OSCC, spanning the entire perioperative course.

Received 20th November 2025,
Accepted 18th January 2026

DOI: 10.1039/d5bm01701g

rsc.li/biomaterials-science

Open Access Article. Published on 06 1404. Downloaded on 21/02/1405 06:57:07 ..
This article is licensed under a Creative Commons Attribution-NonCommercial 3.0 Unported Licence.

1. Introduction

Oral squamous cell carcinoma (OSCC) is one of the most common malignant tumors of the head and neck, characterized by its high invasiveness and tendency for early lymph node metastasis, and remains one of the leading causes of cancer-related deaths worldwide.[1] Although multidisciplinary treatment centered on surgical resection has become the standard treatment, the five-year survival rate for OSCC patients remains around 50%.[2] Among various prognostic indicators, surgical margin status is widely recognized as a decisive factor, where positive margins significantly increase the risk of local recurrence and reduce overall survival.[3–6] Therefore, the success of OSCC surgery largely depends on precise intraoperative assessment of tumor margins.

Current diagnostic and treatment processes remain fragmented and have limitations. Preoperative computed tomography (CT) scans provide valuable three-dimensional anatomical information but cannot offer real-time guidance during surgery.[7] Intraoperatively, surgeons primarily rely on visual inspection and tactile feedback, both of which are highly subjective. While frozen section analysis can provide real-time assessment, its accuracy is affected by sampling errors and time constraints.[8–11] Postoperative histopathology within 24–72 hours remains the gold standard for margin assessment, yet once positive margins are confirmed, it is often difficult to perform re-excision immediately, and adjuvant therapies such as radiotherapy or chemotherapy often cause serious side effects.[12–14] Although standardized treatment protocols for OSCC are in place, their fragmented nature and the lack of intuitive intraoperative guidance tools may be key factors hindering further improvements in patient survival rates.

Near-infrared (NIR) fluorescence imaging (FI) has attracted widespread attention due to its ability to provide real-time visualization during surgery. Fluorescence imaging contrast agents, such as indocyanine green (ICG), have been used for

[a]*Nanjing Stomatological Hospital, Affiliated Hospital of Medical School, Institute of Stomatology, Nanjing University, Nanjing 210008, China.*
E-mail: zywangkq@nju.edu.cn
[b]*College of Materials Engineering, Jinling Institute of Technology, Nanjing 211169, China. E-mail: wangjianquan006@163.com*
† These authors contributed equally to this work.

Open Access Article. Published on 06 1404. Downloaded on 21/02/1405 06:57:07 ..
This article is licensed under a Creative Commons Attribution-NonCommercial 3.0 Unported Licence.

intraoperative guidance in OSCC surgery.[15–17] However, FI alone has inherent limitations: while it excels in delineating superficial lesions, its limited tissue penetration depth and anatomical resolution prevent it from adequately and accurately assessing deep or complex tumor boundaries.[18,19] Furthermore, there is still a pressing need for efficient and minimally invasive treatment alternatives for patients diagnosed with positive surgical margins postoperatively. Against this backdrop, photodynamic therapy (PDT) has emerged as a promising treatment option due to its high selectivity, non-invasiveness, and proven efficacy.[20–22]

In response to this unmet need, we developed a multifunctional probe and established a perioperative strategy for OSCC surgery that enables coordinated management before, during, and after tumor resection. This integrated solution was aimed at providing high-resolution anatomical localization preoperatively, enabling real-time, precise margin navigation intraoperatively, and offering timely, minimally invasive intervention for positive margins postoperatively, thereby providing comprehensive support throughout the OSCC surgical treatment process.

As the most widely used fluorescent dye, ICG has been the subject of continuous optimization and novel application development by researchers in recent years.[23,24] Consistent with this trend, our team has long focused on optimizing ICG-mediated FI in the NIR range. In our previous work, conjugation of ICG with human serum albumin (HSA) markedly enhanced fluorescence stability and tumor-targeting efficiency.[25] Building on this foundation, we developed a multifunctional theranostic nanoplatform, AuNPs/HSA–ICG, composed of clinically established components.[26–31] In this system, biocompatible HSA serves as a stabilizing and targeting carrier, co-encapsulating ICG as a fluorescent dye and photosensitizer, together with gold nanoparticles (AuNPs) as a CT contrast agent.[32–36] Importantly, HSA interacts with secreted protein acidic and rich in cysteine (SPARC), which is widely overexpressed in OSCC, enabling tumor-specific delivery.[37–39] Meanwhile, AuNPs provide excellent CT contrast owing to their high X-ray attenuation and have demonstrated favorable biosafety in previous studies.[34,40]

In recent years, rapid advances in nanotechnology have driven the development of diverse nanoprobes with promising diagnostic and therapeutic performance. For example, gold-based nanomaterials, owing to their unique optical properties, have been widely explored for imaging enhancement as well as photothermal and photodynamic therapy, while multimodal NIR-II probes have enabled highly sensitive imaging of oral tumors and lymph nodes and are often combined with chemotherapy or photothermal therapy to improve therapeutic outcomes.[41,42] However, many existing systems rely on synthetic components and passive targeting mechanisms, and focus primarily on a single diagnostic or therapeutic stage. In contrast, the AuNPs/HSA–ICG nanoplatform developed in this study is composed of components with established clinical relevance and incorporates SPARC-mediated active targeting. More importantly, unlike conventional probes that address only one phase of treatment, our platform is specifically designed to support comprehensive perioperative management by integrating preoperative planning, intraoperative navigation, and postoperative adjuvant therapy, thereby offering a potential approach for bridging the gap in current fragmented clinical protocols.

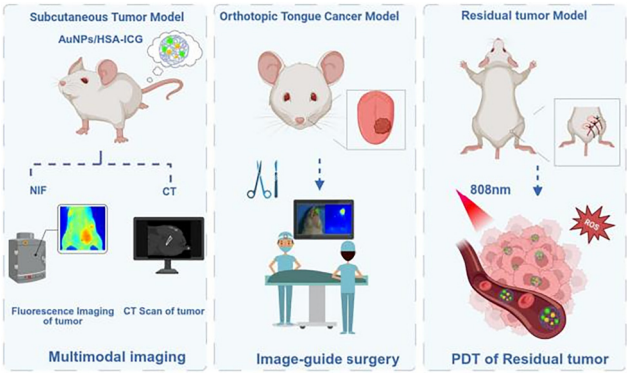

Scheme 1 An integrated AuNPs/HSA–ICG nanoplatform enables a seamless perioperative strategy for OSCC by combining preoperative CT, real-time intraoperative fluorescence navigation, and postoperative PDT to improve surgical margin management.

The core innovation of this study lies in establishing a perioperative, full-process management strategy for OSCC using the AuNPs/HSA–ICG nanoplatform. Specifically, preoperative CT enables precise three-dimensional localization, intraoperative ICG fluorescence provides real-time margin visualization, and postoperative PDT offers a minimally invasive adjuvant therapy for residual tumors. In this work, we detail the design rationale, synthesis, and biological evaluation of the nanoplatform, and demonstrate its robust performance in dual-modal imaging, image-guided surgery, and photodynamic therapy. Collectively, these results highlight its strong translational potential for improving clinical outcomes in OSCC patients with positive surgical margins (Scheme 1).

2. Materials and methods

2.1. Materials

Chloroauric acid ($HAuCl_4$), *meso*-2,3-dimercaptosuccinic acid (DMSA), *N*-hydroxy succinimide (NHS), 1-ethyl-3-(3-dimethylaminopropyl)carbodiimide hydrochloride (EDC), and additional chemicals were obtained from Sigma-Aldrich (St Louis, MO) with analytical-grade purity. ICG was acquired from YiChuang Pharmaceutical Co., Ltd (Dandong, China). CCK-8, the calcein/PI cell viability detection kit, and the reactive oxygen species assay kit were all sourced from Biyuntian Biotechnology Co., Ltd (Shanghai, China).

2.2. Synthesis and characterization of AuNPs/HSA–ICG

First, the ICG–HSA complex was prepared by co-dissolving ICG and HSA powders in PBS at a 1 : 1 mole ratio under continuous stirring (12 h, room temperature, protected from light).

This journal is © The Royal Society of Chemistry 2026

Open Access Article. Published on 06 1404. Downloaded on 21/02/1405 06:57:07 ..
This article is licensed under a Creative Commons Attribution-NonCommercial 3.0 Unported Licence.

AuNPs were synthesized based on a previously reported procedure.[43] Briefly, an aqueous solution of $HAuCl_4$ was prepared. To this solution, DMSA was added under vigorous stirring at a molar ratio of 1 : 2 (Au : DMSA). A gradual color transition from light yellow to brown and then to dark yellow was observed within 10 minutes. Unreacted DMSA and thiolate byproducts were removed by dialysis against DI water for 24 h (Spectra/Por 3, MWCO: 3500). The dialyzed solution was lyophilized to concentrate the nanoparticles. Subsequently, the AuNPs were redissolved in water, and EDC and NHS were added to the solution (molar ratio of EDC : NHS = 1 : 1). The reaction mixture was stirred at 35 °C for 3 hours in the dark. The previously prepared ICG–HSA complex was then introduced into the reaction, and stirring was continued for an additional 24 hours. The resulting AuNPs/HSA–ICG nanocomplex was further purified by dialysis against DI water for 72 hours to remove unreacted components, followed by lyophilization for storage and further use.

The FTIR spectra of the AuNPs/HSA–ICG nanoparticles were acquired from 4000 to 400 cm^{-1} with KBr, performed on a Bruker IFS 66 V vacuum-type spectrometer. UV-vis spectrophotometers (UV-3600i Plus, Shimadzu, Japan) were used to record the UV spectra of AuNPs and AuNPs/HSA–ICG. Dynamic light scattering (BT-90, Dandong Baxter Instrument Co., Ltd Dandong, China) and TEM (Talos F200X G2, FEI, USA) were used to evaluate the NPs' size and nanomorphology. The content of ICG was confirmed using UV-vis spectrophotometers and the Au content was confirmed by ICP-OES/MS (5110 OES, Agilent, USA). FI/CT imaging of materials or animals was performed using an FI system (REAL-IGS, NuoYuan Medical Devices Co., Ltd., Nanjing, China) and Hiscan XM Micro-CT (Suzhou Hiscan Information Technology Co., Ltd). To evaluate the fluorescence stability, PBS solutions of free ICG and AuNPs/HSA–ICG containing equivalent final ICG concentrations were prepared. All samples were stored at room temperature, protected from light. The changes in fluorescence signals were recorded using an FI system every 24 h for 7 consecutive days.

2.3. Cells and animals

All animal experiments were performed in accordance with the guidelines of the Animal Protection Committee of Nanjing University and approved by the Medical Ethics Committee of the Institute of Stomatological Hospital affiliated with Nanjing University Medical School. BALB/c nude male mice (6 weeks old, 18–20 g) were purchased from Changzhou Cavens Experimental Animal Co., Ltd (Jiangsu, China). OSCC cell lines, including CAL27, HSC3 and SCC7, and Human Umbilical Vein Endothelial Cells (HUVEC) were acquired from the Type Culture Collection of the Chinese Academy of Sciences (Shanghai, China).

2.4. Cell uptake experiment

Cells were seeded in 24-well plates and allowed to adhere overnight. Upon reaching 70% confluence, HSC3 and CAL27 cells were treated under identical conditions with either free ICG or AuNPs/HSA–ICG complexes (ICG concentration = 25 μg mL^{-1}) in DMEM supplemented with 10% FBS for 1, 2, and 4 hours at 4 °C or 37 °C. Fluorescence intensity was monitored using an FI system and quantified with ImageJ software.

Given the constraints of our imaging equipment, we conjugated Cy5 fluorescent dye to the AuNPs/HSA–ICG nanocomplexes (AuNPs/HSA–ICG-Cy5) to track cellular uptake *via* confocal microscopy. HSC3 and CAL27 cells were plated in suitable glass-bottomed dishes (1×10^5 cells per dish) and incubated overnight. The cells were then treated with AuNPs/HSA–ICG-Cy5 (ICG concentration = 25 μg mL^{-1}) diluted in DMEM supplemented with 10% FBS for 4 hours at 4 °C or 37 °C, followed by PBS washing, fixation with 4% paraformaldehyde, and DAPI nuclear staining. Confocal laser scanning microscopy was performed using identical imaging settings for both cell lines to assess the relative intracellular fluorescence distribution and intensity. Flow cytometry was used to measure and quantify the staining results.

2.5. Intracellular ROS detection

CAL27 cells were seeded into 12-well plates at a density of 2×10^5 cells per well. The medium was replaced with fresh DMEM containing AuNPs/HSA–ICG nanoparticles (ICG concentration = 9 μg mL^{-1}) the next day. After 4 hours of incubation, the cells were gently washed with PBS and then treated with DCFH-DA (10 μM) for 30 minutes in the dark. After the probe was loaded, the cells were washed again with PBS and exposed to an 808 nm laser at 0.5 W cm^{-2} for 5 minutes. Fluorescence images showing intracellular reactive oxygen species (ROS) were captured immediately using an inverted fluorescence microscope. The mean fluorescence intensity (MFI, a.u.) was calculated from three randomly selected fields per well using ImageJ software to represent the intracellular ROS levels.

2.6. Cell compatibility

The cytotoxicity of AuNPs/HSA–ICG was evaluated *in vitro* using a CCK-8 assay on four cell types (HUVECs, CAL27, HSC3, and SCC7). The cells were seeded into 96-well plates at 5×10^3 cells per well and cultured for 24 hours. They were then treated with different concentrations of AuNPs/HSA–ICG (0, 3, 6, 9, 12.5, 25, and 50 μg mL^{-1}) and incubated for either 24 or 48 hours. After treatment, 100 μL of fresh medium containing 10 μL of CCK-8 solution was added to each well and incubated for 30 minutes. Cell viability was measured at 450 nm using a microplate reader. To further confirm the cytotoxic effects, a live/dead staining assay was performed. Cells were seeded into 12-well plates at 2×10^5 cells per well and cultured for 24 hours. The medium was replaced with fresh medium containing AuNPs/HSA–ICG (ICG = 50 μg mL^{-1}) for different incubation times. After treatment, the cells were washed with PBS and stained with calcein-AM/PI live/dead staining for 30 minutes. Cell viability was then observed using an inverted fluorescence microscope.

2.7. *In vitro* antitumor evaluation

The *in vitro* antitumor effect of AuNPs/HSA–ICG was tested using a similar procedure to that described above. CAL27 cells

Open Access Article. Published on 06 1404. Downloaded on 21/02/1405 06:57:07 ..
This article is licensed under a Creative Commons Attribution-NonCommercial 3.0 Unported Licence.

were seeded into 96-well plates at 5×10^3 cells per well and cultured for 24 hours. The cells were then treated with AuNPs/HSA–ICG and incubated for another 24 hours. After that, they were exposed to an 808 nm laser and kept under normal culture conditions for an additional 6 hours. Cell viability was evaluated using the CCK-8 assay. Cytotoxicity was visually confirmed by calcein-AM/PI live/dead staining, where live and dead cells were stained green and red, respectively. The numbers of live (green) and dead (red) cells in randomly selected fields were counted using ImageJ software. Cell viability was calculated as the percentage of live cells relative to the total cell count.

2.8. Multimodality imaging *in vivo*

To construct the subcutaneous tumor model of BALB/c nude mice, 200 μL of PBS containing 1×10^7 CAL27 cells was injected subcutaneously into the right buttock of the mice. Tumor-bearing mice entered the experimental phase once tumors had reached approximately 100 mm^3.

Mice bearing tumors were randomly divided into two groups (n = 6), and 200 μL of either PBS solution containing free ICG or PBS solution containing AuNPs/HSA–ICG at an equivalent ICG concentration of 1 mg mL^{-1} (corresponding to a dose of 10 mg kg^{-1}) was given intravenously. Fluorescence images were collected at 1, 3, 5, and 24 h post-injection. Following completion of the *in vivo* imaging studies, mice were humanely euthanized and subjected to necropsy for tissue collection. Tumors and major organs (heart, liver, spleen, lungs, and kidneys) were excised for *ex vivo* FI and quantitative assessment of the biodistribution profile of the AuNPs/HSA–ICG.

In terms of CT imaging, Micro-CT was used to scan the mice; specifically, the same dose of drug as mentioned above was injected through the tail vein to obtain CT images at the specified time points.

2.9. Image-guided surgery

We established an orthotopic tongue cancer model in BALB/c nude mice to simulate image-guided surgery. The experimental procedure was as follows: 50 μL of PBS containing 5×10^5 CAL27 cells was injected into the tongue to induce tumor formation. Approximately one week post-inoculation, when supralingual tumors became macroscopically visible, AuNPs/HSA–ICG was administered intravenously at the same dosage as used for the imaging studies. Surgical resection of the tongue tumor was then performed under an FI system and Micro-CT.

2.10. *In vivo* antitumor evaluation

To establish a residual tumor model, mice were anesthetized when subcutaneous tumors reached approximately 100 mm^3. Following the administration of AuNPs/HSA–ICG, the tumor was fully exposed *via* a skin incision, and its major and minor axes were measured using a vernier caliper to calculate the initial dimensions and establish the baseline volume. This partial resection strategy was adapted from a previously reported residual tumor model with minor modifications.[44] Assisted by FI for boundary visualization, approximately 70% of the tumor bulk was surgically resected based on intraoperative volumetric estimation relative to the baseline. Subsequently, FI was utilized to verify the presence of residual tumor tissue (~30% of the initial volume) within the surgical bed prior to wound closure. About 3 d later, bumps appeared under the skin at the site where the tumor had been removed, simulating the clinical scenario of rapid post-operative recurrence. The mice were randomly divided into two groups: a control group without irradiation and a treatment group that received NIR laser irradiation. For the treatment group, AuNPs/HSA–ICG was supplementally injected prior to each laser session, followed by 808 nm laser irradiation (0.5 W cm^{-2}, 5 min) of the residual tumor site, whereas the control group was administered an equivalent volume of PBS solution. Tumor volume was measured and recorded at each time point. After three laser treatments, the mice were sacrificed, and the tumors were collected for further analysis.

2.11. Biocompatibility

To assess systemic biosafety, AuNPs/HSA–ICG was injected intravenously into healthy BALB/c nude mice (n = 6) at an equivalent ICG dose of 20 mg kg^{-1} every other day for 14 days. Another group of mice (n = 6) injected with an equivalent volume of PBS served as the control group. During the treatment period, body weight was monitored regularly. On day 14, the mice were sacrificed, and about 0.8 mL of whole blood was collected for hematology and biochemical tests. Major organs were removed, fixed in 4% formalin, embedded in paraffin, and sectioned for histological analysis. The sections were stained with H&E and examined under a light microscope (Ol Limbass, Germany).

2.12. Data analysis

The statistical analyses were carried out using GraphPad Prism 9.0 software. Data are shown as mean ± standard deviation (SD). Student's t-test was adopted to determine the significant differences. $P < 0.05$ was considered statistically significant.

3. Results

3.1. Characterization and dual-modal imaging properties of AuNPs/HSA–ICG

AuNPs/HSA–ICG was prepared by loading ICG and AuNPs onto HSA, as shown in Fig. 1A. The synthesized AuNPs showed a dark yellow color, and the final AuNPs/HSA–ICG complex appeared dark green, similar to free ICG (Fig. S1). TEM imaging revealed the morphological features of both AuNPs and AuNPs/HSA–ICG (Fig. 1B and C). The average size of the AuNPs was determined by TEM to be 3 ± 0.2 nm, while DLS measurements indicated a hydrodynamic diameter of approximately 10 ± 2 nm, consistent with values reported in the literature. After functionalization with HSA–ICG, the AuNPs/HSA–ICG nanoparticles exhibited a spherical morphology with sizes

 This journal is © The Royal Society of Chemistry 2026

Open Access Article. Published on 06 1404. Downloaded on 21/02/1405 06:57:07 ..
This article is licensed under a Creative Commons Attribution-NonCommercial 3.0 Unported Licence.

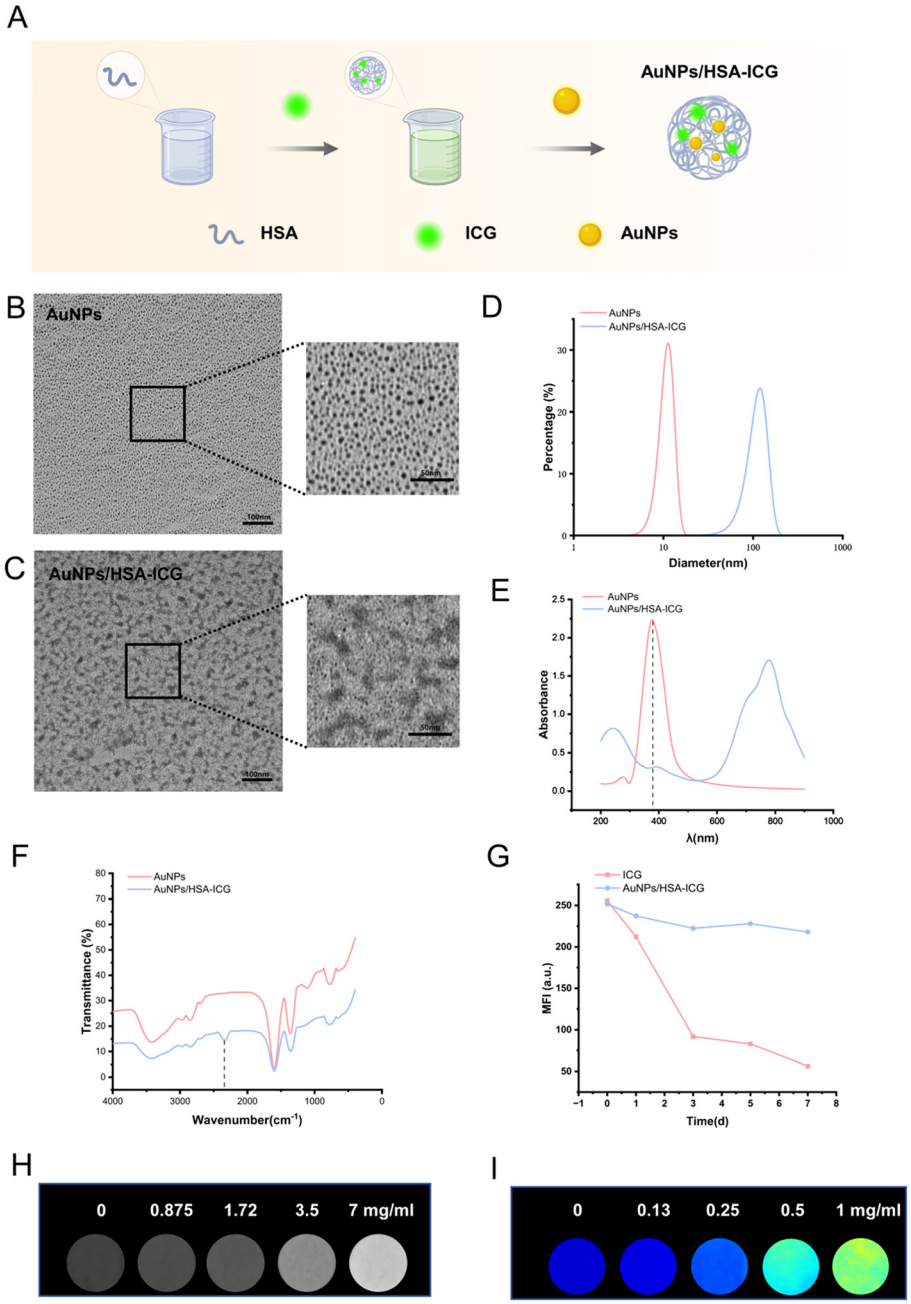

Fig. 1 (A) The preparation process of AuNPs/HSA–ICG. (B and C) TEM images of AuNPs and AuNPs/HSA–ICG. (D) Hydrodynamic size distributions. (E) UV-vis absorption spectra. (F) FTIR spectra. (G) Changes in the fluorescence intensity of free ICG and AuNPs/HSA–ICG incubated in PBS (pH 7.4) at room temperature over a period of 7 days (protected from light). (H) CT image of AuNPs/HSA–ICG. (I) Fluorescence image of AuNPs/HSA–ICG.

ranging from 20 to 50 nm. DLS analysis further showed an increase in the hydrodynamic diameter of AuNPs/HSA–ICG to approximately 100 ± 20 nm, compared to unmodified AuNPs (Fig. 1D).

UV-vis spectroscopy confirmed the characteristic absorption peaks at 390 nm for AuNPs and 790 nm for ICG (Fig. 1E). FTIR analysis (Fig. 1F) demonstrated signature peaks corresponding to HSA, including C═O stretching at 1700 cm^{-1}, C–O stretching at 1300 cm^{-1}, and C═O stretching vibration absorption (overtones) at 3437 cm^{-1}. The characteristic peak at 1110 cm^{-1} can be attributed to the C–O stretching vibration absorption. The appearance of these peaks in the spectrum indicated the successful conjugation of AuNPs to the backbone of HSA. Using UV-vis spectroscopy and a standard curve, the ICG concentration in the AuNPs/HSA–ICG complex was quantified as approximately 1 mg mL^{-1} (Fig. S2). Meanwhile, ICP-OES/MS measurements determined the Au content to be about 7 mg mL^{-1}.

Open Access Article. Published on 06 1404. Downloaded on 21/02/1405 06:57:07 ..
This article is licensed under a Creative Commons Attribution-NonCommercial 3.0 Unported Licence.

The fluorescence stability of AuNPs/HSA–ICG was further assessed *in vitro* (Fig. 1G and Fig. S3). The MFI of both free ICG and AuNPs/HSA–ICG started near 250 a.u., but diverged significantly over 7 days. Free ICG dropped to about 200 a.u. by day 1 and fell sharply to about 80 a.u. by day 3, with a markedly weakened signal. This rapid signal decay is mainly attributed to the intrinsic instability of free ICG in aqueous environments, where it is prone to self-aggregation and chemical degradation, leading to fluorescence quenching. In contrast, AuNPs/HSA–ICG retained strong fluorescence, maintaining an MFI of about 200 a.u. on day 3. The binding of ICG to the hydrophobic domains of HSA effectively prevents molecular aggregation and shields ICG from the surrounding aqueous environment, thereby markedly improving its fluorescence stability.[25] This observation is consistent with the literature and supportive of potential clinical application.

Moreover, the AuNPs/HSA–ICG nanocomplex demonstrated compelling dual-modal imaging properties. As shown in Fig. 1H, AuNPs/HSA–ICG exhibited excellent X-ray attenuation capability. The brightness of the CT images increased consistently with rising Au concentrations. Quantitative analysis confirmed a significant linear positive correlation between the CT value (HU) and the Au concentration (R^2 = 0.9475). Specifically, the CT value reached 99 ± 28 HU at an Au concentration of 0.875 mg mL^{-1} and further escalated to approximately 854 ± 51 HU at 7 mg mL^{-1} (Fig. S4A), demonstrating the superior *in vitro* CT contrast efficacy of the nanoprobe. Similarly, fluorescence intensity showed a concentration-dependent enhancement, with an approximately 5-fold higher MFI at 1 mg mL^{-1} compared to 0.13 mg mL^{-1} (Fig. 1I and Fig. S4B).

In conclusion, we successfully synthesized the nano-theranostic platform, AuNPs/HSA–ICG, which shows excellent FI/CT bimodal imaging capability *in vitro* and lays a foundation for *in vivo* imaging research.

3.2. Cellular uptake mediated by SPARC expression

High expression of SPARC has been demonstrated to be closely associated with poor prognosis in OSCC.[37] Clinical studies have shown that SPARC is significantly overexpressed in the head and neck squamous cell carcinomas, including OSCC, with approximately 60–80% of clinical samples exhibiting positive SPARC staining, compared with normal tissues.[25,45,46] Moreover, SPARC has been reported to specifically bind to HSA.[47]

To investigate the impact of SPARC expression levels on AuNPs/HSA–ICG uptake, uptake assays were performed separately on HSC3 and CAL27 cells, characterized by low and high SPARC expression levels, respectively. FI revealed enhanced fluorescence signals in both cell types as the incubation time increased, with CAL27 cells showing significantly stronger signals than HSC3 cells (Fig. 2A). Quantitative analysis indicated that after 4 hours of incubation, the MFI of CAL27 cells was approximately twice that of HSC3 cells (Fig. 2B). This differential uptake pattern, which was further corroborated by CLSM observations (Fig. 2G) and flow cytometry quantification (Fig. 2H), suggests a positive correlation between cellular internalization and SPARC expression levels.

We further evaluated the uptake efficiency of the nanoplatform compared to free ICG. In CAL27 cells, the AuNPs/HSA–ICG group displayed markedly higher fluorescence intensity than the free ICG group under identical concentrations (Fig. 2C, D and Fig. S5). This suggests that the HSA-based nanostructure facilitates superior intracellular accumulation, likely preventing rapid efflux or degradation associated with the free dye.

Given that active uptake processes require energy, we suppressed cellular metabolism under low temperature conditions (4 °C). Compared to 37 °C, 4 °C markedly reduced cellular uptake of both AuNPs/HSA–ICG and free ICG (Fig. 2E and F). This temperature-dependent inhibition was further corroborated by CLSM imaging and flow cytometry analysis (Fig. 2G and H). Notably, the fluorescence signal of AuNPs/HSA–ICG (by approximately 80%) was significantly reduced, indicating that AuNPs/HSA–ICG primarily entered cells through energy-dependent active pathways such as endocytosis.

In summary, CAL27 cells with high SPARC expression exhibited significantly enhanced uptake of AuNPs/HSA–ICG *via* energy-dependent active pathways. This behavior is likely mediated by specific interactions between HSA and SPARC.

3.3. Cytotoxicity and photodynamic therapeutic efficacy of AuNPs/HSA–ICG *in vitro*

The cytotoxicity of AuNPs/HSA–ICG was evaluated across four cell lines, including HUVECs and three OSCC lines (CAL27, HSC3, and SCC7), using the CCK-8 assay. Even at a high concentration of 50 μg mL^{-1} after 48 hours of exposure, AuNPs/HSA–ICG exhibited minimal cytotoxicity, with all cell lines maintaining over 95% viability (Fig. 3A and Fig. S6). This outstanding biocompatibility was further corroborated by live/dead staining assays, where fluorescence microscopy revealed negligible cell death after 48 hours of continuous treatment at 50 μg mL^{-1} (Fig. S7).

The photosensitizing capability of AuNPs/HSA–ICG was subsequently assessed by detecting intracellular ROS generation using the DCFH-DA probe. While control groups (PBS with or without laser, and AuNPs/HSA–ICG without laser) exhibited only weak background fluorescence, the AuNPs/HSA–ICG + laser group displayed intense green fluorescence after NIR laser irradiation (Fig. 3C). Quantitative analysis confirmed that the MFI of this group was approximately four times higher than that of the untreated AuNPs/HSA–ICG group (Fig. 3D), unequivocally demonstrating efficient ROS generation upon laser excitation.

The *in vitro* antitumor efficacy of AuNPs/HSA–ICG-mediated PDT was then systematically evaluated. The CCK-8 assay was employed to determine the optimal treatment parameters, revealing a progressive reduction in cell viability correlated with increases in drug dose, laser intensity, and exposure duration (Fig. 3B and Fig. S8). Optimal treatment conditions were established as 9 μg mL^{-1} drug concentration, 0.5 W cm^{-2} irradiation power, and 5 min irradiation time, achieving

 This journal is © The Royal Society of Chemistry 2026

Open Access Article. Published on 06 1404. Downloaded on 21/02/1405 06:57:07 ..
This article is licensed under a Creative Commons Attribution-NonCommercial 3.0 Unported Licence.

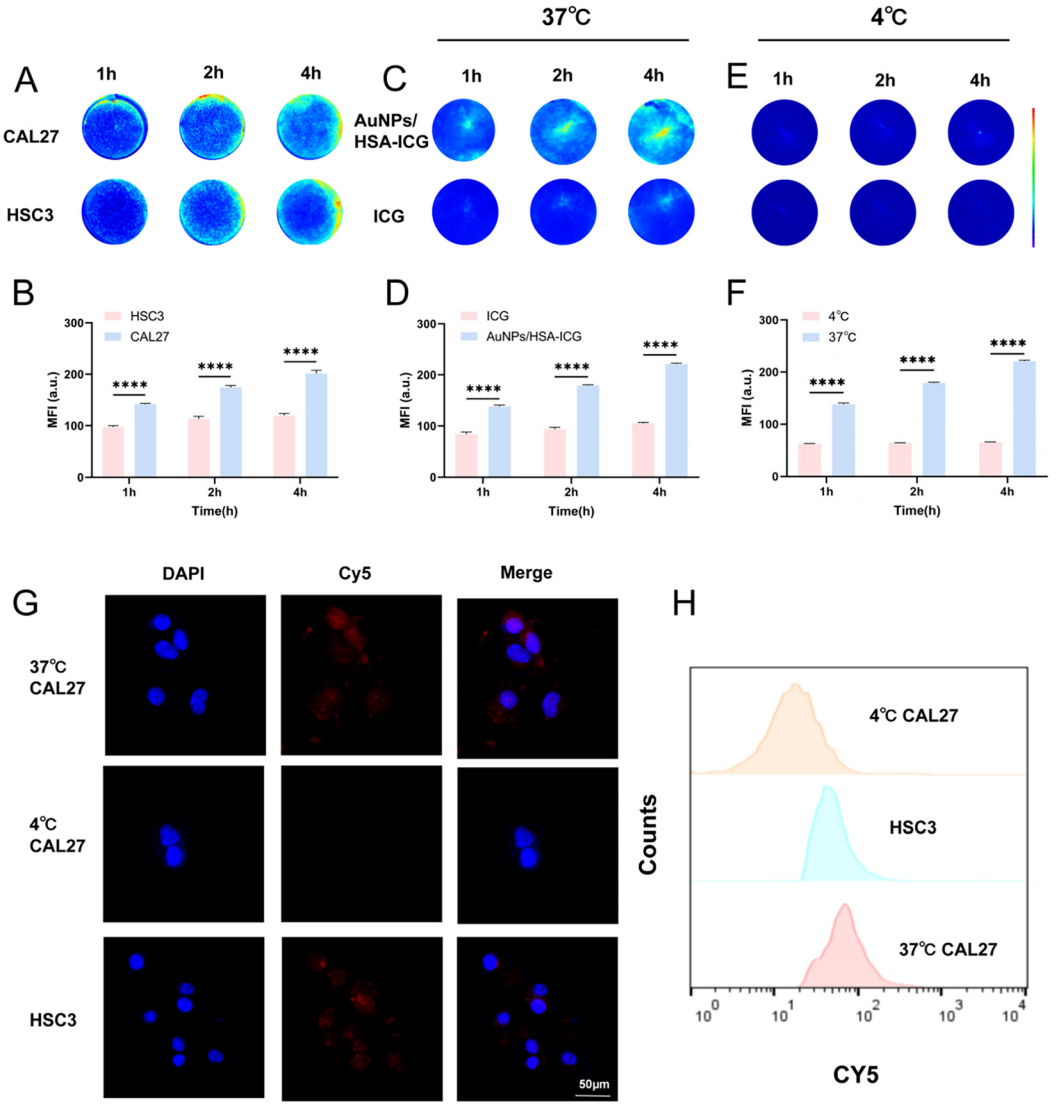

Fig. 2 (A) FI of two different cell lines (CAL27 and HSC3) incubated with AuNPs/HSA–ICG for 1, 2, and 4 h to verify SPARC-mediated uptake (Ex/Em = 785/825 nm, exposure time = 0.3 s). (B) Quantitative analysis of MFI shown in (A). (C) FI of CAL27 cells incubated with different reagents (free ICG and AuNPs/HSA–ICG) at 37 °C to demonstrate the enhanced uptake of the nanocomplex. (D) Quantitative analysis of MFI shown in (C). (E) FI of CAL27 cells incubated with different reagents (free ICG and AuNPs/HSA–ICG) at 4 °C. The suppressed fluorescence signal at low temperature indicates that the cellular uptake of the nanocomplex is mediated by an energy-dependent pathway. (F) Quantitative analysis of the MFI of CAL27 cells treated with AuNPs/HSA–ICG at 37 °C and 4 °C. (G) CLSM images of CAL27 and HSC3 cells incubated with AuNPs/HSA–ICG. (H) The cellular uptake of AuNPs/HSA–ICG was determined by flow cytometry. Values represent means ± SD, $n = 3$. ***$p < 0.001$.

approximately 50% cell death without excessive toxicity. Live/dead staining under these conditions revealed abundant red fluorescence (indicating dead cells) specifically in the AuNPs/HSA–ICG + laser group (Fig. 3E), with quantitative analysis showing less than 25% viable cells (Fig. 3F). Together, these results demonstrate that AuNPs/HSA–ICG exerts an excellent PDT effect on OSCC cells *in vitro*.

3.4. *In vivo* dual-modal imaging and biocompatibility

To evaluate the dual-modal imaging capabilities of AuNPs/HSA–ICG, tumor-bearing nude mice were administered intravenous injection of the nanoplatform *via* the tail vein.

For FI, whole-body signals were monitored for up to 24 hours using an FI system. As shown in Fig. 4A, at 1 h post-injection, fluorescence in the free ICG group was primarily localized in the liver and other organs, whereas the AuNPs/HSA–ICG group showed significant accumulation at the tumor site. While the fluorescence signals in both groups gradually decreased over time due to metabolic clearance, the AuNPs/HSA–ICG group exhibited consistently superior tumor retention compared to the rapid washout observed in the free ICG group. Semi-quantitative analysis showed that tumor fluorescence intensity in the AuNPs/HSA–ICG group was significantly higher than that of the free ICG group at 1 h, yielding a

Open Access Article. Published on 06 1404. Downloaded on 21/02/1405 06:57:07 ..
This article is licensed under a Creative Commons Attribution-NonCommercial 3.0 Unported Licence.

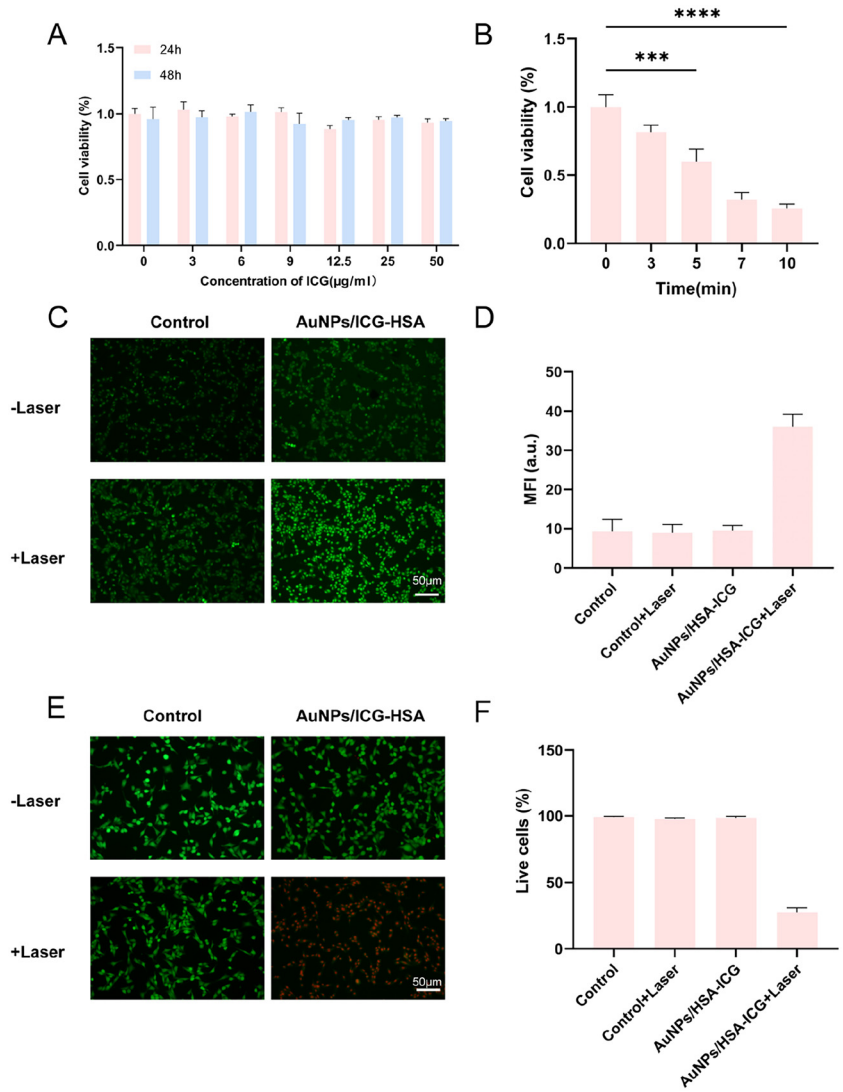

Fig. 3 (A) Cytoviability of CAL27 cells after incubation with AuNPs/HSA–ICG at various concentrations (0, 3, 6, 9, 12.5, 25, and 50 μg mL^{-1}) for 24 and 48 h, respectively. (B) Changes in cell viability after laser irradiation for different exposure times (0, 3, 5, 7, and 10 min) (ICG concentration = 9 μg mL^{-1}, 0.5 W cm^{-2}). (C) Inverted fluorescence micrographs of ROS generation after laser irradiation (ICG concentration = 9 μg mL^{-1}, 808 nm laser, 0.5 W cm^{-2} for 5 min). (D) Quantitative analysis of (C). (E) The inverted fluorescence micrographs of live/dead staining (ICG concentration = 9 μg mL^{-1}, 808 nm laser, 0.5 W cm^{-2} for 5 min). Red indicates dead cells and green indicates live cells. (F) Quantitative analysis of (E). Values represent means ± SD, $n = 3$. ***$p < 0.001$.

satisfactory SBR that facilitated clear tumor visualization (Fig. 4B and C). After *in vivo* imaging, animals were sacrificed, and the tumors along with major organs were excised for *ex vivo* FI, which confirmed prominent accumulation of AuNPs/HSA–ICG in the tumor, liver, and kidney tissues (Fig. 4D and E).

To assess the CT imaging performance, mice were scanned at multiple time points post-injection using Micro-CT. As illustrated in Fig. 4F, the tumor margins were clearly defined as early as 1 hour, with contrast intensity increasing over time due to progressive tumor-site accumulation. As shown in Fig. S9, quantitative monitoring confirmed a continuous accumulation pattern, where the tumor CT radiodensity gradually rose over time, ultimately reaching a maximum intensity of 204 ± 7HU at 12 h. These results indicate that AuNPs/HSA–ICG provides excellent *in vivo* contrast enhancement for CT imaging. In summary, AuNPs/HSA–ICG exhibits excellent FI/CT dual-modal imaging capabilities *in vivo*.

The excellent dual-modal imaging performance of AuNPs/HSA–ICG highlights its potential for clinical translation, thus we further investigate its *in vivo* biocompatibility, laying the foundation for the clinical translation of AuNPs/HSA–ICG (Fig. 5A).

Mice treated with AuNPs/HSA–ICG showed a body weight profile comparable to that of the control group (Fig. 5B). Hematological parameters, including erythrocyte, leukocyte, and platelet counts, remained within normal physiological

 This journal is © The Royal Society of Chemistry 2026

Open Access Article. Published on 06 1404. Downloaded on 21/02/1405 06:57:07 ..
This article is licensed under a Creative Commons Attribution-NonCommercial 3.0 Unported Licence.

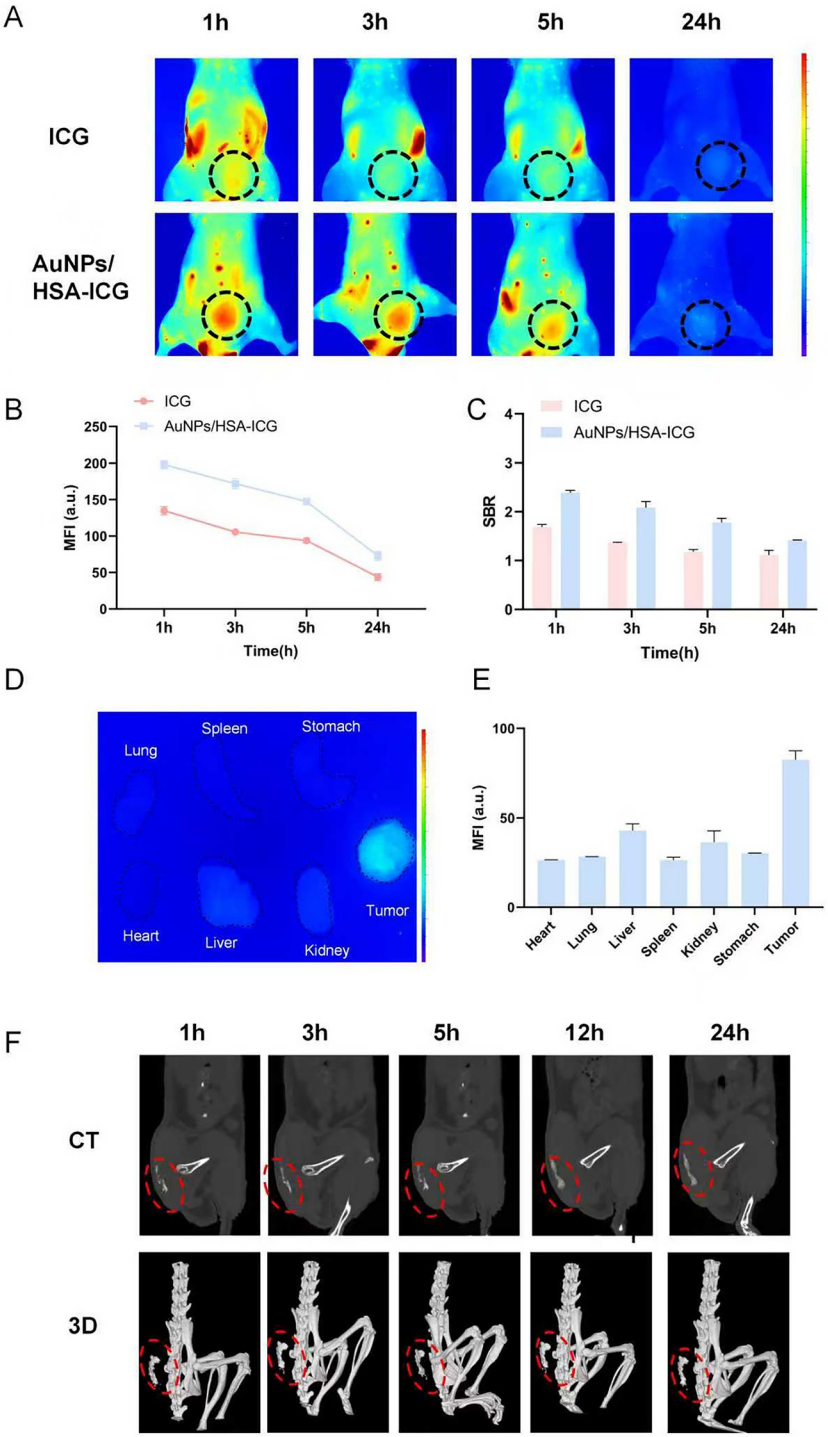

Fig. 4 (A) Representative fluorescence images of subcutaneous tumor-bearing mice at 1, 3, 5, and 24 h post-injection (Ex/Em = 785/825 nm). (B) MFI of the images shown in (A). (C) Signal to background ratio (SBR) of the tumor site shown in (A), calculated using the surrounding normal tissue as the background. (D) *Ex vivo* fluorescence images of tumors and major organs excision at 24 h post-injection. (E) Quantitative analysis of the tumor and major organs shown in (D). (F) Representative CT images of the subcutaneous tumors in mice at 1, 3, 5, 12 and 24 h post-injection.

ranges throughout the study. Additionally, blood biochemistry analyses revealed no significant alterations in liver or kidney function markers (Fig. 5C and Fig. S10, S11). Histopathological examination of major organs revealed no structural abnormalities, tissue damage, or signs of inflammation (Fig. 5D). These collective findings confirm the excellent biosafety and biocompatibility of AuNPs/HSA–ICG, robustly supporting its potential for further translational development.

Open Access Article. Published on 06 1404. Downloaded on 21/02/1405 06:57:07 ..
This article is licensed under a Creative Commons Attribution-NonCommercial 3.0 Unported Licence.

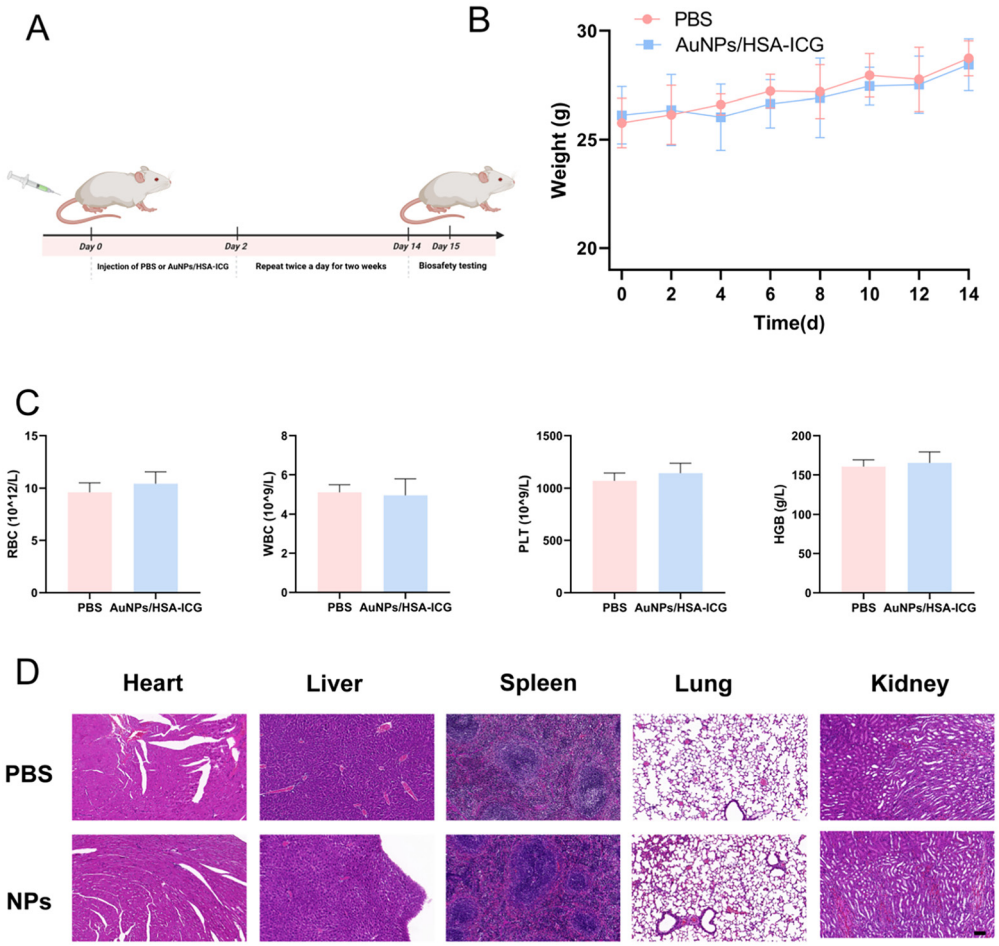

Fig. 5 (A) Schematic diagram of the biological safety assessment process. (B) Average body weight curves of mice in the PBS and AuNPs/HSA–ICG groups monitored over a 14-day period. (C) Blood hematology data. (D) Representative H&E stained images of the major organs collected from the mice treated with PBS or AuNPs/HSA–ICG at day 15 post-injection. The scale bar is 100 μm, ×100.

3.5. Image-guided surgery

Based on the above results, AuNPs/HSA–ICG demonstrated excellent biosafety and dual-modal (FI/CT) imaging capabilities. We next evaluated its clinical utility in an orthotopic tongue cancer model simulating a complete surgical procedure, aiming to elucidate the synergistic benefits of bimodal imaging for residual tumor detection (Fig. 6A).

Approximately one hour after injection of AuNPs/HSA–ICG, the simulated surgical procedure was initiated. Preoperative CT imaging clearly delineated the tumor's three-dimensional boundaries, providing detailed anatomical guidance, while FI concurrently highlighted superficial lesions (Fig. 6B). Initially, an attempt was made to remove the tumor without fluorescence guidance. After the grossly visible tumor tissue was excised, FI of the surgical site revealed residual areas emitting specific green fluorescence. Subsequent CT scans showed abnormally dense shadows within the surgical area (Fig. 6C). A fluorescence-guided extended resection was then performed to remove all tissues emitting green fluorescence. Repeat fluorescence and CT imaging confirmed the absence of any abnormal signals (Fig. 6D). Quantitative analysis confirmed a drastic reduction in fluorescence intensity in the tumor bed post-resection, dropping to background levels (Fig. S12). Pathological examination of the excised tissues confirmed that all removed specimens were tumor tissue and no residual tumor remained in the surgical bed (Fig. 6E and Fig. S13).

3.6. *In vivo* antitumor effect

In the previous sections, we confirmed the utility of AuNPs/HSA–ICG for preoperative planning and intraoperative navigation in OSCC. Here, we further evaluate its potential application as a postoperative intervention for OSCC with positive margins.

Building upon previous *in vitro* findings confirming strong photodynamic activity under 808 nm laser irradiation, a residual tumor model was established in mice to assess *in vivo* performance (Fig. 7A and Fig. S14). Following surgical resection, the NIR treatment group received repeated photodynamic treatments. Despite tumor volume increasing in both groups over time, growth in the NIR treatment group was significantly

 This journal is © The Royal Society of Chemistry 2026

Open Access Article. Published on 06 1404. Downloaded on 21/02/1405 06:57:07 ..
This article is licensed under a Creative Commons Attribution-NonCommercial 3.0 Unported Licence.

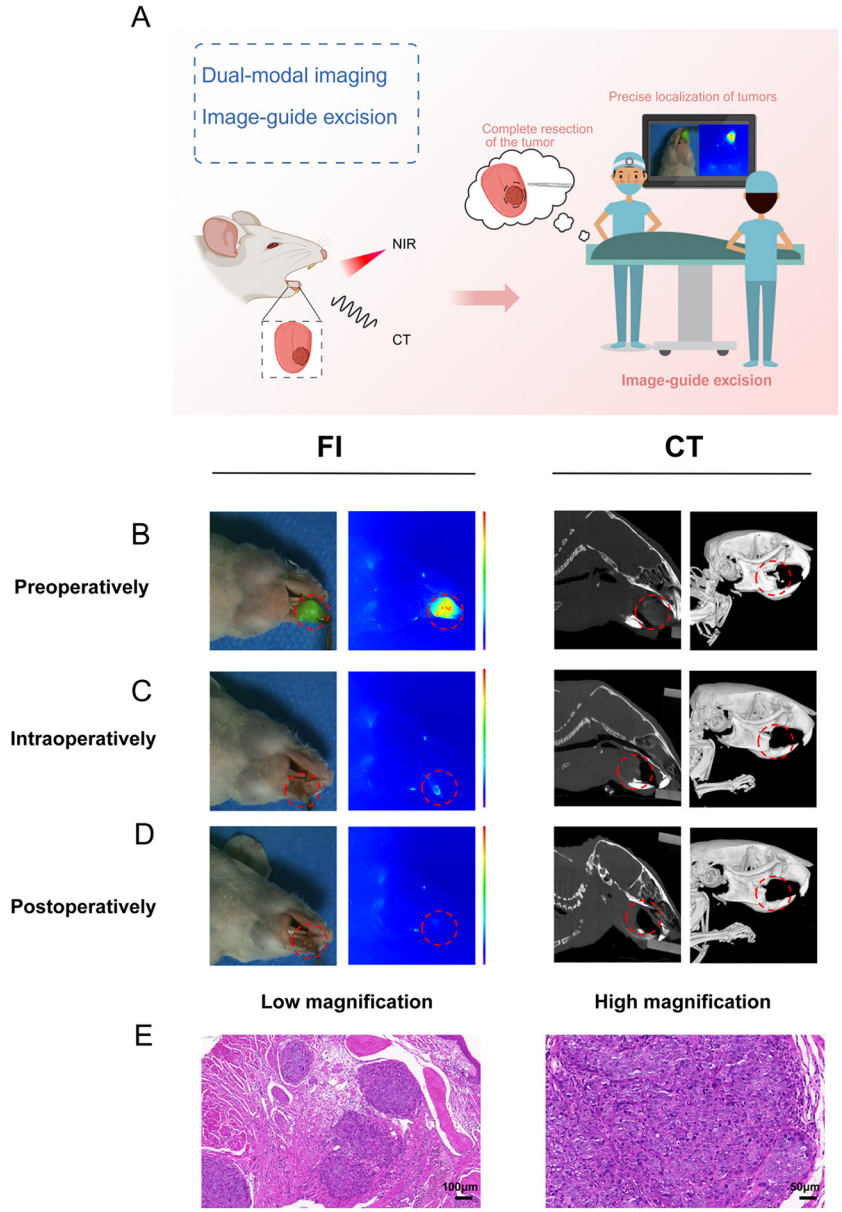

Fig. 6 (A) Schematic diagram of bimodal image-guided surgery. (B) Preoperative FI/CT images. (C) Intraoperative FI/CT images. (D) Postoperative FI/CT images. (E) Representative H&E staining images of tumor tissues excised from the orthotopic tongue cancer model. Scale bars: 100 μm (low magnification, ×100) and 50 μm (high magnification, ×200).

inhibited (Fig. 7B and C). After three irradiation sessions, the anatomy showed that tumors in the control group were highly invasive and irregularly shaped, whereas those in the NIR treatment group remained more regular and spherical. Quantitative analysis revealed that tumor weight was markedly reduced in the treatment group (Fig. 7D and E). H&E staining further confirmed greater tumor cell apoptosis in the NIR treatment group (Fig. 7F). These results indicate that AuNPs/HSA–ICG has significant antitumor effects on tumors *in vivo* under near-infrared light excitation. Notably, there were no significant differences in body weight or hematological indices between the two groups during treatment (Fig. S15–S18), and no deaths or obvious adverse reactions occurred in the NIR treatment group, which fully confirmed the *in vivo* safety of the therapy. Although the tumors in the experimental group were not completely eliminated within 7 days, their growth was effectively controlled. In conclusion, AuNPs/HSA–ICG-mediated photodynamic therapy demonstrates potential as a minimally invasive, safe, and targeted approach to inhibit residual tumor growth.

4. Discussion

Surgical margin status is a decisive prognostic factor in OSCC. However, existing diagnostic and therapeutic modalities remain functionally fragmented across preoperative planning,

Open Access Article. Published on 06 1404. Downloaded on 21/02/1405 06:57:07 ..
This article is licensed under a Creative Commons Attribution-NonCommercial 3.0 Unported Licence.

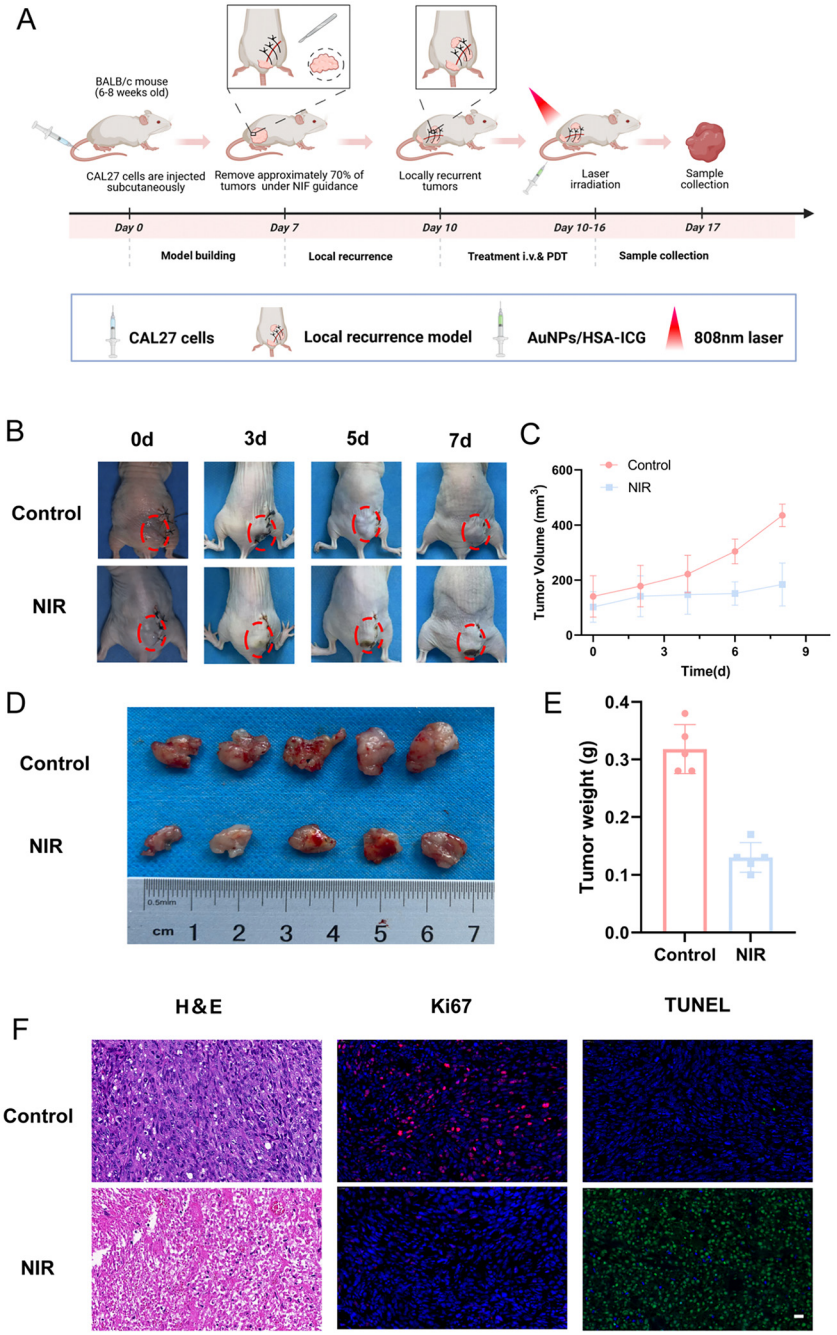

Fig. 7 (A) Schematic diagram of PDT for residual tumors in mice. (B) Representative photographs of tumor-bearing mice in the control and NIR treatment groups during the treatment period (days 0, 3, 5, and 7). Day 0: surgical resection and day 3: first laser irradiation. (C) Tumor volume curves of the different groups. (D) Photograph of the isolated tumor after the end of treatment. (E) Histogram of tumor weight comparison between the two groups after different treatments. (F) H&E, TUNEL, and Ki67 staining of the tumor slices. The scale bar is 20 μm, ×400.

intraoperative navigation, and postoperative intervention, thereby limiting further improvement in patient outcomes. In this study, we developed an HSA-based theranostic nanoplatform that integrates dual-modal imaging and photodynamic therapy, offering a unified approach for both diagnosis and treatment. This strategy facilitates continuous perioperative management, encompassing preoperative assessment, intraoperative guidance, and postoperative therapy in OSCC.

Unlike conventional theranostic systems that simply combine diagnostic and therapeutic functions, this platform is designed to support a continuous and coordinated workflow spanning preoperative planning, intraoperative guidance, and postoperative intervention.[48–51] Preoperatively, AuNP-enabled CT imaging provides high-resolution three-dimensional anatomical information for surgical planning. Intraoperatively, near-infrared fluorescence from HSA-stabilized ICG enables

 This journal is © The Royal Society of Chemistry 2026

Open Access Article. Published on 06 1404. Downloaded on 21/02/1405 06:57:07 ..
This article is licensed under a Creative Commons Attribution-NonCommercial 3.0 Unported Licence.

real-time visualization of tumor margins. The complementary integration of CT-based depth information and fluorescence-guided surface delineation offers enhanced intraoperative guidance compared to single modalities. In our orthotopic tongue cancer model, this dual-modal strategy provided critical visual cues that facilitated the macroscopic complete resection of the primary tumor, demonstrating the platform's potential to enhance surgical precision.

Positive surgical margins are a primary driver of rapid local recurrence in OSCC, a clinical challenge specifically simulated in our residual tumor model. In this context, postoperative PDT is positioned not as a standalone curative modality, but as a targeted adjuvant intervention designed to manage residual disease post-resection. In our *in vivo* assessment, AuNPs/HSA–ICG-mediated PDT significantly inhibited tumor regrowth within the surgical bed and delayed recurrence compared to the control group. These results substantiate the potential of this platform as a localized adjuvant strategy. In contrast to the systemic toxicity of chemotherapy or the high invasiveness associated with aggressive reoperation, this approach offers a precise, minimally invasive therapeutic modality to manage residual lesions. In summary, this strategy facilitates a continuous perioperative continuum spanning precise localization, resection, and targeted suppression of residual disease, thereby providing a novel and feasible approach to managing the complex issue of positive surgical margins.

The multifunctionality of the platform stems from the rational design of its components. HSA not only stabilizes ICG and enhances fluorescence performance but also mediates SPARC-dependent active targeting, contributing to both high imaging contrast and improved therapeutic response. The use of clinically validated building blocks (HSA, ICG, and AuNPs) further supports translational potential, which was confirmed through systematic biocompatibility evaluations.

Nevertheless, certain limitations must be acknowledged. While the combined CT and FI successfully guided surgery in the murine orthotopic tongue cancer model, the anatomical complexity of the human head and neck and the high cost of intraoperative CT limit direct clinical translation. Future implementation may therefore rely on AI-assisted image fusion techniques, integrating high-resolution preoperative CT with real-time intraoperative fluorescence to overcome tissue penetration limits.[52] The dual-signal capability of AuNPs/HSA–ICG provides the material foundation for achieving this vision. Second, in our mouse model, the growth of residual tumors was effectively suppressed but not completely eliminated. This outcome may be attributed to the surgical disruption of local blood flow, which limits the optimum accumulation of nanoparticles, the limited penetration depth of light, and the short observation period of only seven days, among other factors. Despite incomplete eradication, the treatment effectively controlled tumor growth in a safe and noninvasive manner. This suggests that AuNPs/HSA–ICG-mediated PDT may be best utilized as a precise, minimally invasive adjuvant therapy, particularly for patients who are unsuitable for aggressive resection or chemoradiotherapy due to health conditions, tumor location, or personal preference.[53–56] Such an approach could help control disease progression, prolong survival, and improve quality of life. Further optimization of dosing, irradiation parameters, or combination with other therapeutic modalities could enhance efficacy. Finally, although no acute toxicity was observed in this study, gold nanoparticles are known for potential long-term persistence in biological systems, and long-term follow-up is necessary to rule out potential delayed adverse effects.

5. Conclusion

In this study, we developed an AuNPs/HSA–ICG nanoplatform composed of clinically established components and proposed an innovative perioperative management strategy for OSCC that integrates preoperative CT planning, intraoperative fluorescence navigation, and postoperative PDT. Systematic *in vitro* and *in vivo* evaluations demonstrated the platform's excellent dual-modal imaging capabilities, significant tumor suppression, and favorable biocompatibility. Using various animal models, we simulated and validated its complete translational pathway from diagnosis to therapy. Nevertheless, certain limitations of this study should be acknowledged. Looking ahead, integrating preoperative CT data with intraoperative FI through artificial intelligence-based algorithms could enable real-time three-dimensional surgical navigation and overcome the depth limitations of FI. Although PDT did not achieve complete ablation of residual tumors, it demonstrated potential as a minimally invasive adjuvant treatment for selected patient populations. Further optimization of treatment parameters and exploration of combination therapies may enhance efficacy. Additionally, long-term biosafety will require evaluation through extended follow-up studies.

Author contributions

D. S.: conceptualization, investigation, methodology, and writing – original draft. D. X.: conceptualization, investigation, methodology, and writing – review and editing. L. Z.: investigation and visualization. J. W.: language, conceptualization, resources, and project administration. Z. W.: conceptualization, supervision, review and editing, and funding acquisition. All authors read and approved the final manuscript.

Conflicts of interest

The authors declare that they have no known competing financial interests or personal relationships that could have appeared to influence the work reported in this paper.

Ethics approval

All animal experiments were performed in accordance with the guidelines of the Animal Protection Committee of Nanjing

Open Access Article. Published on 06 1404. Downloaded on 21/02/1405 06:57:07 ..
This article is licensed under a Creative Commons Attribution-NonCommercial 3.0 Unported Licence.

University and approved by the Medical Ethics Committee of the Institute of Stomatological Hospital affiliated with Nanjing University Medical School (approval no. JX-2024-NL44).

Data availability

All data generated or analyzed during this study are included in this published article and will be available from the corresponding author upon reasonable request.

Supplementary information (SI) is available. See DOI: https://doi.org/10.1039/d5bm01701g.

Acknowledgements

This study was supported by the Nanjing Health Science and Technology Development Project (YKK24200), the High Level Hospital Construction Research Project (0224C007), Jiangsu Provincial Clinical Key Specialty Construction Project, and the Foundation of Jinling Institute of Technology (no. jit-b-202219).

References

1 R. L. Siegel, K. D. Miller, H. E. Fuchs and A. Jemal, *CA: A Cancer J. Clin.*, 2021, **71**, 7–33.
2 L. Q. M. Chow, *N. Engl. J. Med.*, 2020, **382**, 60–72.
3 D. Brinkman, D. Callanan, R. O'Shea, H. Jawad, L. Feeley and P. Sheahan, *Oral Oncol.*, 2020, **110**, 104883.
4 Y. Pu, Y. Wang, X. Huang, S. Chen, Z. Wang, G. Sun, E. Tang, S. Zhao, Y. Ni and Q. Hu, *Int. J. Oral Maxillofac. Surg.*, 2016, **45**, 1372–1377.
5 V. Mutlu, H. Ucuncu, E. Altas and B. Aktan, *Eurasian J. Med.*, 2014, **46**, 1–7.
6 P. J. Slootweg, G. J. Hordijk, Y. Schade, R. J. J. van Es and R. Koole, *Oral Oncol.*, 2002, **38**, 500–503.
7 L. J. Forrest, *Vet. Clin. North Am.: Small Anim. Pract.*, 2016, **46**, 499–513.
8 I. Tessler, V. Marilena, E. E. Alon, N. A. Gecel, E. Remer, I. Gluck, T. Yoffe and A. Dobriyan, *Laryngoscope*, 2024, **134**, 1725–1732.
9 A. Singh, B. Qayyumi and P. Chaturvedi, *Curr. Oncol. Rep.*, 2020, **22**, 82.
10 L. Ferrari, F. Pérez Salazar, P. Cariati, J. Fernández Solis, R. M. Pulgar Encinas, S. Ferrari and I. Martínez Lara, *J. Craniomaxillofac. Surg.*, 2025, **53**, 840–843.
11 R. N. Spence, V. Efthymiou, D. Goss and M. A. Varvares, *Oral Oncol.*, 2023, **147**, 106609.
12 H. Y. Sroussi, J. B. Epstein, R.-J. Bensadoun, D. P. Saunders, R. V. Lalla, C. A. Migliorati, N. Heaivilin and Z. S. Zumsteg, *Cancer Med.*, 2017, **6**, 2918–2931.
13 S. T. Sonis, *Oral Oncol.*, 1998, **34**, 39–43.
14 J. E. Raber-Durlacher, A. Barasch, D. E. Peterson, R. V. Lalla, M. M. Schubert and W. E. Fibbe, *Supportive Cancer Ther.*, 2004, **1**, 219–229.
15 Y. Zhu, T. Xiao, Y. He, X. Hong, T. Zhou, M. Da, S. Ge, D. Xie and Z. Wang, *Front. Cell Dev. Biol.*, 2022, **10**, 986575.
16 Y.-J. Lee, G. Krishnan, N. Nishio, N. S. van den Berg, G. Lu, B. A. Martin, S. van Keulen, A. D. Colevas, S. Kapoor, J. T. C. Liu and E. L. Rosenthal, *Laryngoscope*, 2021, **131**, 529–534.
17 J. Pan, H. Deng, S. Hu, C. Xia, Y. Chen, J. Wang and Y. Wang, *World J. Surg. Oncol.*, 2020, **18**, 96.
18 L. Zhang, Y. Wang, Z. Peng, Y. Weng, Z. Fang, F. Xiao, C. Zhang, Z. Fan, K. Huang, Y. Zhu, W. Jiang, J. Shen and R. Zhan, *Int. J. Biol. Sci.*, 2022, **18**, 3458–3469.
19 R. Yang, Q. X. Li, C. Mao, X. Peng, Y. Wang, Y. X. Guo and C. B. Guo, *Beijing Daxue Xuebao, Yixueban*, 2019, **51**, 53–58.
20 W. Zhang, S. Chen, Z. Bai, M. Gan, M. Chen, Y. Zhang, S. Liu and D. Liu, *Int. J. Nanomed.*, 2024, **19**, 10699–10710.
21 V. Vander Poorten, J. Meulemans, S. Nuyts, P. Clement, R. Hermans, E. Hauben and P. Delaere, *World J. Surg. Oncol.*, 2015, **13**, 214.
22 S. A. Mosaddad, R. A. Namanloo, S. S. Aghili, P. Maskani, M. Alam, K. Abbasi, F. Nouri, E. Tahmasebi, M. Yazdanian and H. Tebyaniyan, *Med. Oncol.*, 2023, **40**, 91.
23 D. Hu, M. Zha, H. Zheng, D. Gao and Z. Sheng, *Research*, 2025, **8**, 0583.
24 X. Xiang, X. Feng, S. Lu, B. Jiang, D. Hao, Q. Pei, Z. Xie and X. Jing, *Exploration*, 2022, **2**, 20220008.
25 Y. Wang, D. Xie, J. Pan, C. Xia, L. Fan, Y. Pu, Q. Zhang, Y. H. Ni, J. Wang and Q. Hu, *Biomater. Sci.*, 2019, **7**, 5270–5282.
26 Y. Yu, T. Yang and T. Sun, *Nanomedicine*, 2020, **15**, 1127–1145.
27 J. Zhang, C. Yang, R. Zhang, R. Chen, Z. Zhang, W. Zhang, S.-H. Peng, X. Chen, G. Liu, C.-S. Hsu and C.-S. Lee, *Adv. Funct. Mater.*, 2017, **27**, 1605094.
28 S. Singh, G. Giammanco, C.-H. Hu, J. Bush, L. S. Cordova, D. J. Lawrence, J. L. Moran, P. V. Chitnis and R. Veneziano, *Photoacoustics*, 2023, **29**, 100437.
29 Y. Lian, F. Feng, X. Meng, Y. Hu, M. Huo, G. Wang and J. Li, *Biomater. Sci.*, 2023, **11**, 4907–4915.
30 P. H. Kee and D. Danila, *Nanomedicine*, 2018, **14**, 1941–1947.
31 L. E. Cole, R. D. Ross, J. M. Tilley, T. Vargo-Gogola and R. K. Roeder, *Nanomedicine*, 2015, **10**, 321–341.
32 B. Liu, C. Li, G. Chen, B. Liu, X. Deng, Y. Wei, J. Xia, B. Xing, P. Ma and J. Lin, *Adv. Sci.*, 2017, **4**, 1600540.
33 W. Fan, P. Huang and X. Chen, *Chem. Soc. Rev.*, 2016, **45**, 6488–6519.
34 X. Song, W. Zhu, X. Ge, R. Li, S. Li, X. Chen, J. Song, J. Xie, X. Chen and H. Yang, *Angew. Chem., Int. Ed.*, 2021, **60**, 1306–1312.
35 D. Wang, J. Yue, Q. Cao, J. Liu, L. Yang, W. Shen, W. Zhang and J. Liu, *Biomater. Sci.*, 2022, **11**, 248–262.
36 X. Hu, J. Li, Y. Chen, Q. Long, Y. Bai, R. Li, K. Wang, M. Jiang, C. Chen, J. Mao, Y. Zheng and Z. Gao, *ACS Biomater. Sci. Eng.*, 2022, **8**, 4535–4546.
37 Y. Jing, Y. Jin, Y. Wang, S. Chen, X. Zhang, Y. Song, Z. Wang, Y. Pu, Y. Ni and Q. Hu, *J. Cell Physiol.*, 2019, **234**, 15581–15593.
38 H. J. Jang, M. G. Song, C. R. Park, H. Youn, Y.-S. Lee, G. J. Cheon and K. W. Kang, *Int. J. Mol. Sci.*, 2023, **24**, 850.

 This journal is © The Royal Society of Chemistry 2026

Open Access Article. Published on 06 1404. Downloaded on 21/02/1405 06:57:07 ..
This article is licensed under a Creative Commons Attribution-NonCommercial 3.0 Unported Licence.

39 K. Park, *J. Controlled Release*, 2012, **157**, 3.
40 E. C. Dreaden, A. M. Alkilany, X. Huang, C. J. Murphy and M. A. El-Sayed, *Chem. Soc. Rev.*, 2012, **41**, 2740–2779.
41 Y. Wang, W. Zhang, P. Sun, Y. Cai, W. Xu, Q. Fan, Q. Hu and W. Han, *Theranostics*, 2019, **9**, 391–404.
42 X. Zhu, J. Chen, J. Zhao, Z. Zhang and C. Wang, *Int. J. Nanomed.*, 2025, **20**, 13689–13719.
43 Y. Negishi and T. Tsukuda, *J. Am. Chem. Soc.*, 2003, **125**, 4046–4047.
44 L. S. Moore, E. De Boer, J. M. Warram, M. D. Tucker, W. R. Carroll, M. L. Korb, M. S. Brandwein-Gensler, G. M. Van Dam and E. L. Rosenthal, *Cancer Med.*, 2016, **5**, 1526–1534.
45 J. S. Lewis, W. L. Thorstad and M. Hussaini, *Appl. Immunohistochem. Mol. Morphol.*, 2022, **30**, 317–325.
46 N. Desai, V. Trieu, B. Damascelli and P. Soon-Shiong, *Transl. Oncol.*, 2009, **2**, 59–64.
47 C. R. Park, J. H. Jo, M. G. Song, J. Y. Park, Y.-H. Kim, H. Youn, S. H. Paek, J.-K. Chung, J. M. Jeong, Y.-S. Lee and K. W. Kang, *Theranostics*, 2019, **9**, 7447–7457.
48 M. Haribabu, V. Guruviah and P. Yogarajah, *Curr. Med. Imaging*, 2023, **19**, 673–694.
49 F. Liu, Q. Kang, H. Xiao, Y. Liu, S. Tan, K. Fan, J. Peng, X. Tan, G. Wu and Q. Yang, *J. Nanobiotechnol.*, 2025, **23**, 235.
50 J. Song, H. Wang, X. Meng, W. Li and J. Qi, *Nat. Commun.*, 2024, **15**, 10395.
51 L. Hang, H. Li, M. Li, Y. Sun, W. Wu, L. Fang, Y. Diao, H. Qu, T. Zhang, S. Li and G. Jiang, *Theranostics*, 2024, **14**, 6671–6691.
52 S. P. Yadav and S. Yadav, *Med. Biol. Eng. Comput.*, 2020, **58**, 669–687.
53 S. Gupta, A. Singh, S. Deorah and A. Tomar, *Crit. Rev. Oncol. Hematol.*, 2025, **209**, 104672.
54 S.-H. Huang and B. O'Sullivan, *Med. Oral Patol. Oral Cir. Bucal*, 2013, **18**, e233–e240.
55 J. A. Woolgar and A. Triantafyllou, *Oral Oncol.*, 2005, **41**, 1034–1043.
56 P. D. Grime, R. Haskell, I. Robertson and R. Gullan, *Int. J. Oral Maxillofac. Surg.*, 1991, **20**, 285–290.